EXTENDED PDF FORMAT SPONSORED BY
Tools for Your
Biological Target
sigma.com/biotarget2

Large-Pore Apertures in a Series of Metal-Organic Frameworks

Hexiang Deng *et al.*

Science **336**, 1018 (2012);
DOI: 10.1126/science.1220131

This copy is for your personal, non-commercial use only.

If you wish to distribute this article to others, you can order high-quality copies for your colleagues, clients, or customers by clicking here.

Permission to republish or repurpose articles or portions of articles can be obtained by following the guidelines here.

The following resources related to this article are available online at www.sciencemag.org (this information is current as of May 30, 2012):

Updated information and services, including high-resolution figures, can be found in the online version of this article at:
http://www.sciencemag.org/content/336/6084/1018.full.html

Supporting Online Material can be found at:
http://www.sciencemag.org/content/suppl/2012/05/23/336.6084.1018.DC1.html

This article **cites 37 articles**, 5 of which can be accessed free:
http://www.sciencemag.org/content/336/6084/1018.full.html#ref-list-1

This article appears in the following **subject collections:**
Chemistry
http://www.sciencemag.org/cgi/collection/chemistry

Science (print ISSN 0036-8075; online ISSN 1095-9203) is published weekly, except the last week in December, by the American Association for the Advancement of Science, 1200 New York Avenue NW, Washington, DC 20005. Copyright 2012 by the American Association for the Advancement of Science; all rights reserved. The title *Science* is a registered trademark of AAAS.

Downloaded from www.sciencemag.org on May 30, 2012

of larger ones—show that, even in systems where OA is dominant, Ostwald ripening can play a role.

In all examples, nanoparticles explored multiple configurations before attachment occurred. This was possible because the primary particles tended to aggregate into clusters where they interacted in close proximity for sufficient periods of time to become nearly aligned through Brownian motion (fig. S3 and movie S1). This tendency implies the existence of a long-range attractive force that is necessary to keep them in proximity. Osmotic forces, which largely drive colloidal stabilization (*30*), are most likely responsible. Previous ex situ studies of OA also proposed this as a source of initial aggregation (*5*); however, this colloidal stabilization must be sufficiently weak to allow the nanoparticles to approach each other within the primary minimum of the interaction potential, where van der Waals interactions could lead to further attraction. In addition, the diffusional dynamics must be sufficiently rapid to allow rearrangement into low-energy configurations. Because the OA event is accompanied by a jump to contact only after orientation is established (Fig. 1), OA is ultimately driven by a short-range force that acts over <1 nm and is highly sensitive to orientation. The orientation dependence would seem to argue for Coulomb interactions as the source of this force, although one cannot rule out van der Waals interactions with anisotropic polarizability. The observation that the acceleration phase occurs over the last 0.5 to 1 nm is consistent with the expected Debye length for a 50 mM 3:1 electrolyte solution (*30*). In addition, the fact that the particles tend to remain separated by nanometer-scale distances until a correct configuration is reached implies the existence of a slight energetic barrier. This provides further support for the importance of electrostatic interactions, which, in the case of molecular crystals such as iron oxides, would produce cation-cation and anion-anion repulsion when the lattices are mismatched.

Irrespective of its source, to estimate the strength of this short-range attraction, we determined the translational and angular acceleration by measuring the frame-to-frame velocity and rotation rate (Fig. 3A). Using the density of ferrihydrite and the measured particle size to determine the mass and moment of inertia for spherical particles, we calculated that the forces and torques acting on the approaching particle arising from particle-attraction are almost completely offset by the resistance of the solution (supplementary text). Even so, the potential energy for the particle-particle interaction, which equals 1.6×10^{-19} J, far exceeds the initial kinetic energy of 7.5×10^{-40} J. In addition, if we assume that this interaction energy is due to the electrostatic force, we find that the particles interact with an effective number of fundamental charges (1.6×10^{-19} C) on the order of unity (supplementary text).

References and Notes

1. Y. Politi *et al.*, *Science* **306**, 1161 (2004).
2. C. E. Killian *et al.*, *J. Am. Chem. Soc.* **131**, 18404 (2009).
3. H. Cölfen, M. Antonietti, *Angew. Chem. Int. Ed.* **44**, 5576 (2005).
4. H. Cölfen, M. Antonietti, *Mesocrystals and Non-classical Crystallization* (Wiley, San Francisco, CA, 2008).
5. J. F. Banfield *et al.*, *Science* **289**, 751 (2000).
6. Y. Yadong, P. Alivisatos, *Nature* **437**, 7059 (2005).
7. K. S. Cho *et al.*, *J. Am. Chem. Soc.* **127**, 7140 (2005).
8. J. Zhang *et al.*, *Nanoscale* **2**, 18 (2010).
9. S. Mann, *Biomineralization: Principles and Concepts in Bioinorganic Materials Chemistry* (Oxford Univ. Press, Oxford, 2001).
10. R. L. Penn, J. F. Banfield, *Science* **281**, 969 (1998).
11. V. M. Yuwono *et al.*, *J. Am. Chem. Soc.* **132**, 2163 (2010).
12. R. L. Penn, J. F. Banfield, *Am. Mineral.* **83**, 1077 (1998).
13. S. A. Hackney, F. S. Biancaniello, D. N. Yoon, C. A. Handwerker, *Scr. Metall.* **20**, 937 (1986).
14. C. W. Passchier, R. A. J. Trouw, *Microtectonics* (Springer, Sturtz, Wurzburg, Germany, 1998).
15. Materials and methods are available as supplementary materials on *Science* Online.
16. R. L. Penn *et al.*, *J. Phys. Chem. B* **105**, 2177 (2001).
17. C. Frandsen *et al.*, *Phys. Rev. B* **72**, 214406 (2005).
18. Y. Yang *et al.*, *Inorg. Chem.* **50**, 10143 (2011).
19. J. C. Joubert, *Anal. Quim.* **93**, S70 (1997).
20. N. Deo, K. A. Natarajan, *Int. J. Miner. Process.* **55**, 41 (1998).
21. R. L. Penn *et al.*, *Geology* **29**, 843 (2001).
22. H. Zheng *et al.*, *Science* **324**, 1309 (2009).
23. D. E. Janney *et al.*, *Clays Clay Miner.* **48**, 111 (2000).
24. R. W. Balluffi *et al.*, *Surf. Sci.* **31**, 68 (1972).
25. G. Hasson *et al.*, *Surf. Sci.* **31**, 115 (1972).
26. V. Randle, *Role of the Coincidence Site Lattice in Grain Boundary Engineering* (Maney Materials Science, London, 1996).
27. R. L. Penn, *J. Phys. Chem. B* **108**, 12707 (2004).
28. C. Ribeiro *et al.*, *ChemPhysChem* **6**, 690 (2005).
29. G. Cao, *Nanostructures and Nanomaterials: Synthesis, Properties and Applications* (Imperial College Press, London, 2004).
30. J. N. Israelachvili, *Intermolecular and Surface Forces* (Academic Press, Waltham, MA, 2011).

Acknowledgments: We thank V. Altoe and S. Aloni for their assistance with electron microscopy and L. Zhang for his help with analysis of the data. This research was supported by the U.S. Department of Energy, Office of Basic Energy Sciences (OBES), by LBNL under contract no. DE-AC02-05CH11231 and Lawrence Livermore National Laboratory (LLNL) under contract DE-AC52-07NA27344. Development of the TEM fluid cell was supported by the OBES, Division of Chemical, Biological and Geological Sciences; analysis of iron oxide formation was supported by the OBES, Division of Materials Science and Engineering; and cell fabrication and TEM analysis were performed at the Molecular Foundry, LLNL, which is supported by the OBES, Scientific User Facilities Division. M.H.N. acknowledges government support under and awarded by the Department of Defense, the Air Force Office of Scientific Research, and a National Defense Science and Engineering Graduate Fellowship, 32 CFR 168a. C.F. acknowledges support from The Danish Council for Independent Research. Data are available in the supplementary materials.

Supplementary Materials

www.sciencemag.org/cgi/content/full/336/6084/1014/DC1
Materials and Methods
Supplementary Text
Figs. S1 to S5
Table S1
References (*31–33*)
Movies S1 to S6

25 January 2012; accepted 27 March 2012
10.1126/science.1219643

Large-Pore Apertures in a Series of Metal-Organic Frameworks

Hexiang Deng,[1]* Sergio Grunder,[2]* Kyle E. Cordova,[1] Cory Valente,[2]
Hiroyasu Furukawa,[1] Mohamad Hmadeh,[1] Felipe Gándara,[1] Adam C. Whalley,[2] Zheng Liu,[3]
Shunsuke Asahina,[4] Hiroyoshi Kazumori,[4] Michael O'Keeffe,[1] Osamu Terasaki,[5,6,7]
J. Fraser Stoddart,[2,7] Omar M. Yaghi[1,7]†‡

We report a strategy to expand the pore aperture of metal-organic frameworks (MOFs) into a previously unattained size regime (>32 angstroms). Specifically, the systematic expansion of a well-known MOF structure, MOF-74, from its original link of one phenylene ring (I) to two, three, four, five, six, seven, nine, and eleven (II to XI, respectively), afforded an isoreticular series of MOF-74 structures (termed IRMOF-74-I to XI) with pore apertures ranging from 14 to 98 angstroms. All members of this series have non-interpenetrating structures and exhibit robust architectures, as evidenced by their permanent porosity and high thermal stability (up to 300°C). The pore apertures of an oligoethylene glycol–functionalized IRMOF-74-VII and IRMOF-74-IX are large enough for natural proteins to enter the pores.

Porous crystals are useful because they allow access of molecules through their pore apertures for storage, separation, or conversion. The pore apertures dictate the size of the molecules that may enter the pores, which provide the surface and space to carry out these functions. A long-standing challenge is to make crystals whose pore apertures are of a size suitable for the inclusion of large organic, inorganic, and biological molecules. The largest reported pore aperture is 32 by 24 Å, and the largest reported internal pore diameter is 47 Å, both of which are found in metal-organic frameworks (MOFs) (*1*, *2*). In principle, it should be possible to use longer links in the synthesis of MOFs so as to provide for even larger pore apertures. However, attempts to do so often yield either interpenetrating structures (*3*, *4*), restricting the size of the pore aperture, or fragile frameworks that collapse upon removal of guests (*1*, *3*).

Here, we report that these challenges are overcome by the expansion of a well-known MOF structure, MOF-74 (*5*, *6*), M_2(2,5-DOT) (where M is Zn^{2+},Mg^{2+} and DOT is dioxidoterephthalate) (Fig. 1, I), from the original DOT link of one phenylene ring to two (II), three (III), four (IV), five (V), six (VI), seven (VII), nine (IX), and eleven (XI) to give an isoreticular (having the same topology) series of MOF-74 structures (termed IRMOF-74-I to -XI), with the dimension of the pore apertures ranging from 14 to 98 Å. Six members of this series (IRMOF-74-IV to -XI) have the largest pore apertures reported to date for a crystalline material, and one member (IRMOF-74-XI), in its guest-free form, has the lowest density (0.195 g cm^{-3}) known thus far for a crystal at room temperature. All members of this series have noninterpenetrating structures and exhibit robust architectures, as evidenced by their permanent porosity and high thermal stability (up to 300°C). We further report experiments indicating that large molecules—such as vitamin B_{12}, metal-organic polyhedron-18, myoglobin, and green fluorescent protein (GFP)—can pass through the pore apertures of IRMOF-74-IV, V, VII, and IX, respectively.

Mesoporous silica, porous carbon, and other related materials are known to have very large apertures (up to 100 nm), and their pore size can be varied in the scale of a few nanometers (*7*–*10*). Unlike these mesoporous materials, the formation of MOFs is governed by the precise linkage of organic struts with the metal atoms to form the secondary building unit (SBUs) (*11*). The formation of the SBUs imposes the precise disposition of the links. In this way, the pore aperture of MOFs can be controlled on the angstrom level through the gradual increase in the number of atoms in the organic links used in the MOF design. These features, coupled with the flexibility in which the MOFs' composition and structure metrics can be varied (*11*–*19*), make them highly desirable for well-defined inclusion processes and indeed distinguish them from other mesoporous materials.

Our strategy for making MOFs with large-pore apertures and avoiding the problem of interpenetration is to start with a framework in which one can maintain a short axis with the long organic links inclined to that axis. The short axis effectively eliminates the possibility of interpenetration because it is the distance between the links along that axis joining the SBUs (*20*, *21*). Ideal in this regard are the frameworks built from infinite rod-shaped metal oxide SBUs, as exemplified in the structure of MOF-74 (Fig. 1A) (*5*, *6*). Here, the metal oxide rod SBUs are in a hexagonal arrangement, joined along the short and long axes by metal-oxygen bonds and organic DOT links, respectively. The formation of the short axis is ensured by the coordination of the metal to the carboxylic and the *ortho*-positioned hydroxyl functionalities of the DOT links, which in turn generates tight packing of the links at an intersecting angle to this axis (fig. S1) (*22*). The resulting product is an extended framework composed of channels along the direction of the short axis that are isolated by walls formed by the aforementioned packing of the organic links, a construct that forbids interpenetration regardless of the organic link's length [(*22*), section S1].

Initially, we produced models of a MOF-74 structure with progressively longer links II to XI. Considering that the composition of the inorganic SBU remains unaltered throughout the entire series, we used the atomic coordinates of the already known MOF-74 structure (*6*) and simply added the appropriate number of phenylene units for each respective member of the series in order to develop the crystal models. All members of this isoreticular series inherit the **etb** net of the parent MOF-74 topology (*23*). The models for IRMOF-74-II and -III were built in $R\bar{3}$, the same space group as for the original MOF-74, whereas for the other members of the series we created the models in *R*3 to better describe the torsion angles

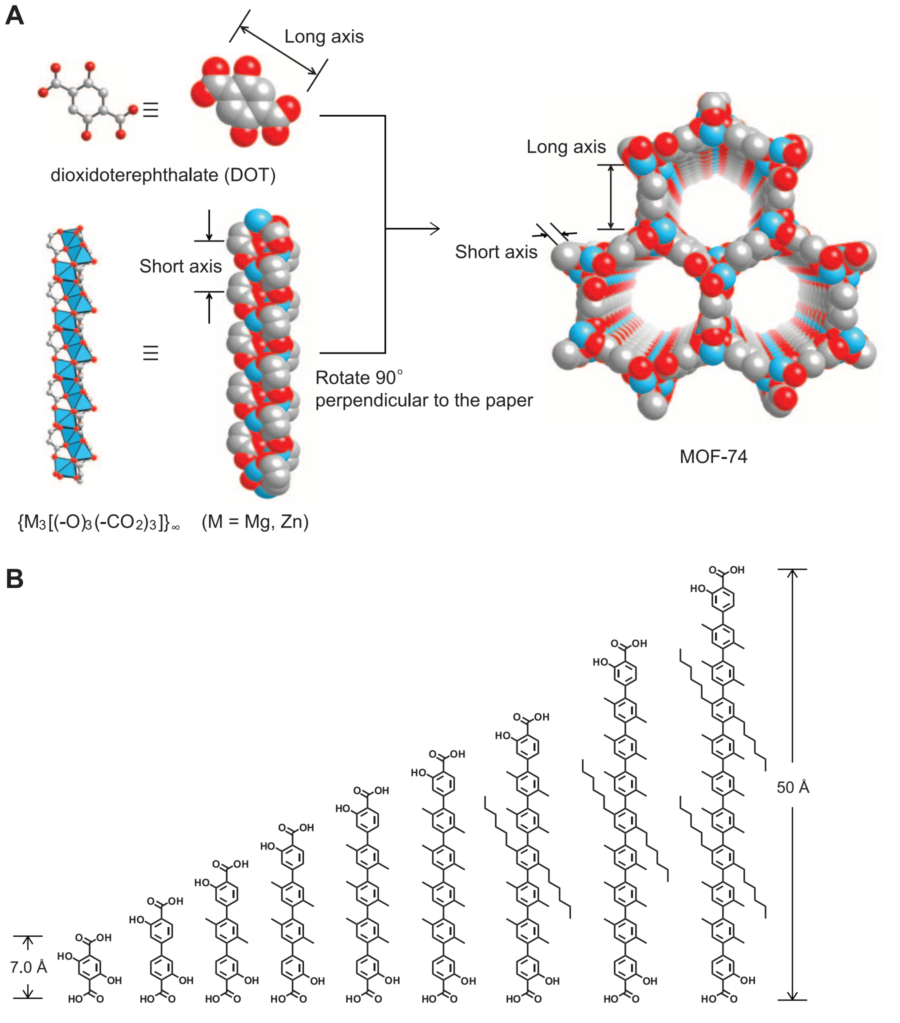

Fig. 1. (**A**) Crystal structure of MOF-74. DOT link is joined by a metal oxide SBU to make the three-dimensional MOF-74 structure with one-dimensional hexagonal channels. C atoms are shown in gray, O atoms are shown in red, 5-coordinate Mg or Zn atoms with open metal sites are shown in blue, and H atoms and terminal ligands protruding into the pores are omitted for clarity. (**B**) Chemical structure of organic links used in the synthesis of a series of nine IRMOFs.

---

[1]Center for Reticular Chemistry, Center for Global Mentoring, University of California, Los Angeles (UCLA)–U.S. Department of Energy (DOE) Institute for Genomics and Proteomics, and the Department of Chemistry and Biochemistry, UCLA, Los Angeles, CA 90095, USA. [2]Center for the Chemistry of Integrated Systems, Department of Chemistry, Northwestern University, Evanston, IL 60208, USA. [3]Nanotube Research Center, National Institute of Advanced Industrial Science and Technology (AIST), Tsukuba 305-0046, Japan. [4]SMBU, JEOL, Akishima, Tokyo 196-8558, Japan. [5]Department of Materials and Environmental Chemistry, Stockholm University, Stockholm 10691, Sweden. [6]EXSELENT, Stockholm University, Stockholm 10691, Sweden. [7]NanoCentury KAIST Institute and Graduate School of Energy, Environment, Water, and Sustainability (World Class University), Daejeon 305-701, Republic of Korea.

*These authors contributed equally to this work.

†Present address: Department of Chemistry, University of California and The Molecular Foundry at Lawrence Berkeley National Laboratory, Berkeley, CA 94720, USA.

‡To whom correspondence should be addressed. E-mail: yaghi@berkeley.edu

that are now present in the links. A molecular mechanics energy minimization was then performed to optimize the geometry of the links within the framework. This approach allowed us to calculate for the IRMOF series the powder x-ray diffraction patterns (PXRDs), their expected cell parameters, pore aperture, and other related porosity information (table S1) (*22*). This initial analysis was followed by the preparation of the links as well as by carrying out the synthesis and characterization of the IRMOFs and comparing the observed and calculated structural data to verify that the entire IRMOF series has the original MOF-74 topology.

In our design of the organic links, a homologous series of palindromic oligophenylene derivatives terminated with α-hydroxy-carboxylic acid functions were targeted to afford linear and robust building blocks for expanding the MOF-74 structure. The notoriously low solubilities of the parent oligophenylenes (*24*) were circumvented by introducing (III to VI) pairs of methyl substituents with *para* dispositions onto all but the terminal phenylene rings in order to introduce torsional twists between the planes of the rings. This stereoelectronic control breaks interring conjugation and reduces π-π stacking (*25*), enhancing the solubilities of the building blocks for IRMOF production [(*22*), section S2]. In the syntheses of the longer links (VII to XI), solubilities were maintained by replacing, in a constitutionally symmetrical manner, selected pairs of methyl groups with hexyl substituents on appropriate phenylene rings. These crucial design criteria, coupled with a modular synthetic strategy, based on transition-metal catalyzed cross-coupling reactions, enabled the efficient elaboration of a series of slender and robust organic links with lengths ranging from 7 (I) to 50 Å (XI) (Fig. 1B). Gram quantities of soluble organic links II to XI were synthesized in 5 to 16 steps [(*22*), section S2].

The synthetic procedures for the IRMOF-74 series were developed on the basis of conditions previously used in the synthesis of the parent MOF-74 (*5*, *6*). As an illustrative example, colorless microcrystalline powder of IRMOF-74-II was isolated from the reaction of a mixture containing $Mg(NO_3)_2{\cdot}6H_2O$, link II, *N*,*N*-dimethylformamide, ethanol, and water at 120°C for 24 hours (90% yield based on the organic link). Similar conditions, with some adopted changes, were used to

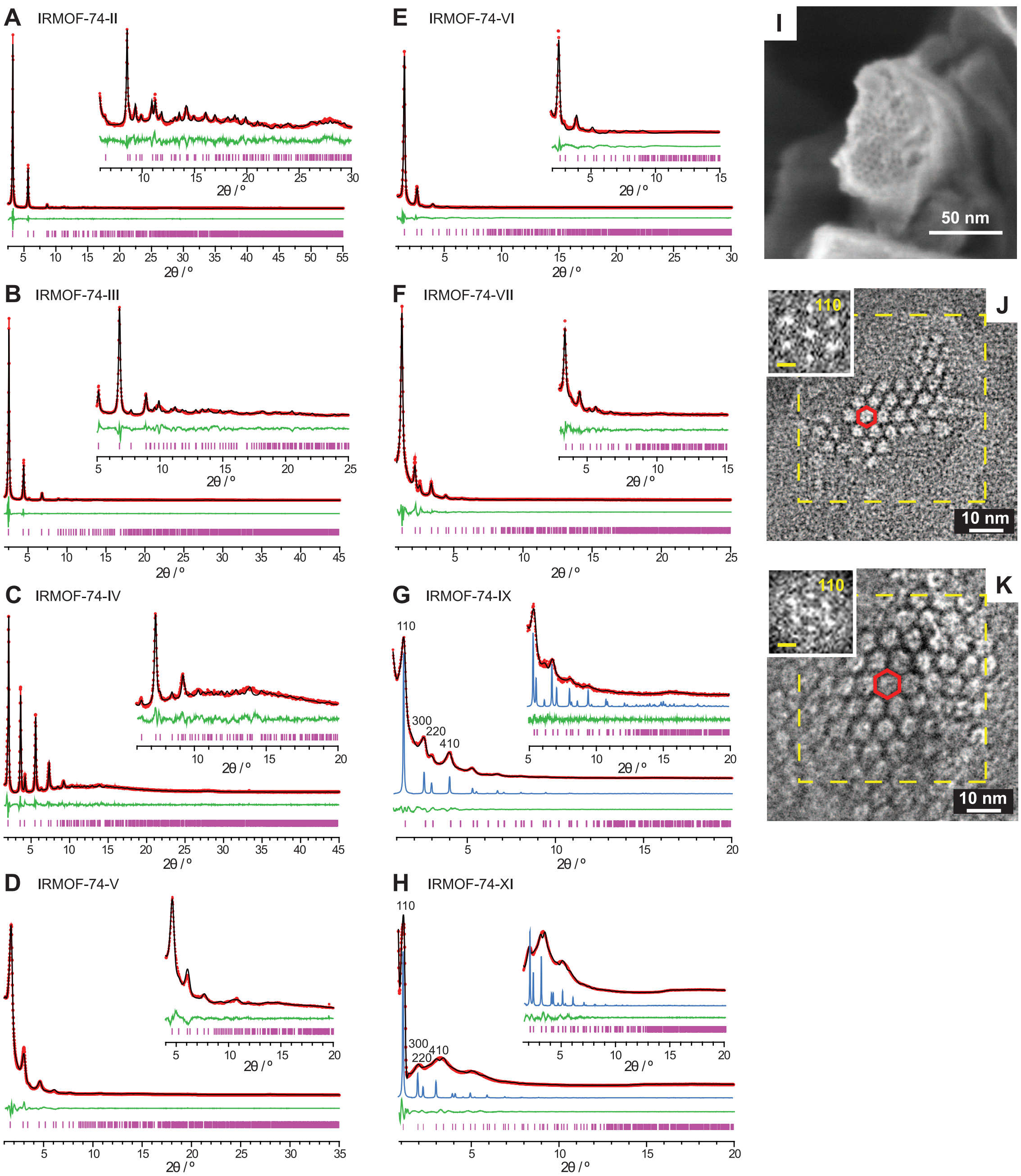

Fig. 2. X-ray diffraction patterns of IRMOF-74 series. (**A** to **F**) The Rietveld refinements of IRMOF-74-II to -VII. (**G** and **H**) The Pawley refinements of IRMOF-74-IX and -XI. Shown are the experimental (red), refined (black), and difference (green) patterns. The Bragg positions are marked as pink bars, and the patterns calculated from the crystal models are shown in blue in (G) and (H). (**I**) HRSEM image of a crystal of IRMOF-74-VII. (**J** and **K**) HRTEM images of IRMOF-74-VII and -IX, respectively. (Insets) The corresponding FFT diffraction patterns of the dashed square area in the original images. Scale bar, 0.2 nm^{-1}.

synthesize the rest of the series in gram quantities and 50 to 95% yield [(*22*), section S3]. The phase purity of each material was confirmed by the singular nature of its needle-like crystal morphology as observed in the scanning electron microscopy (SEM) images [(*22*), section S3]. The materials are highly crystalline, as demonstrated by their sharp powder x-ray diffraction peaks (Fig. 2). However, repeated attempts to produce crystals of the IRMOFs sufficiently large for single-crystal x-ray analysis were unsuccessful. Comparison of the experimental PXRD patterns with those calculated from the crystal models is in good agreement with regard to both positions and the relative intensities of the peaks. The predicted IRMOF-74 structures were ultimately validated with the Rietveld refinements performed for IRMOF-74-II to -VII (Fig. 2, A to H, respectively). The structural parameters were refined against the PXRD patterns collected with a synchrotron source, resulting in satisfactory residuals (table S2) [(*22*), section S4]. IRMOF-74-IX and -XI display broad peaks in their PXRD patterns—indicative of small crystals—a situation that precludes distinguishing the peaks with low intensities in the high-angle area. Furthermore, a possible lessening in the extent of order within the pore walls cannot be ruled out because these members of the series are constructed from extremely long organic links with long alkyl chains in which disorder and flexibility of the links are more pronounced. Although the quality of the diffraction patterns for these members does not allow us to perform a meaningful full structural refinement (Rietveld), the patterns clearly show the most intense diffraction peaks, corresponding to the largest *d*-spacings, at their expected 2θ positions. Accordingly, we carried out Pawley refinements in order to obtain their unit cell information. Low convergence residuals were achieved in the refinements of both compounds, and the agreement of the measured and model-calculated cell parameters indicated the formation of the targeted crystal structures (tables S2 and S3) (*22*).

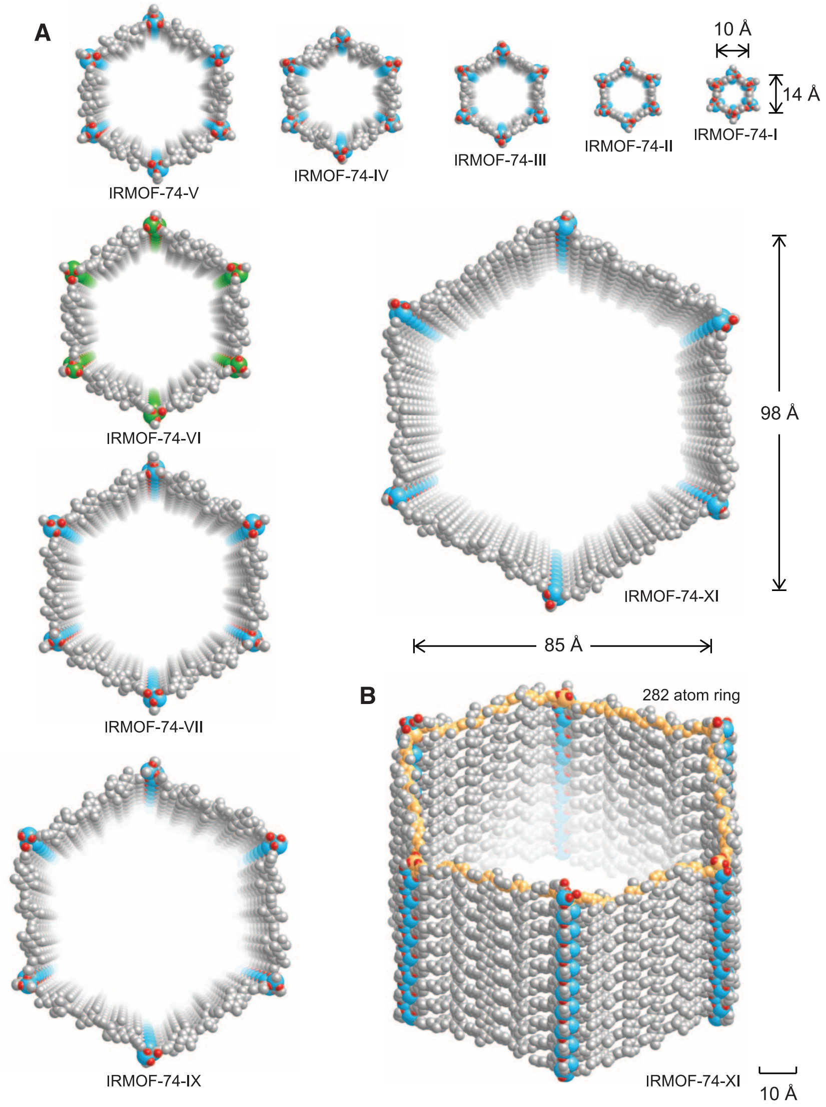

Fig. 3. Crystal structures of IRMOF-74 series. (**A**) Perspective views of a single one-dimensional channel shown for each member of IRMOF series, starting from the smallest (top right). Pore aperture is described by the length of the diagonal and the distance between the two opposite edges in the regular hexagonal cross section. Hexyl chains as well as hydrogen atoms are omitted for clarity. C atoms are shown in gray, O atoms in red, Mg atoms in blue, and Zn atoms in green. (**B**) Perspective side view of the hexagonal channel, showing the ring of 282 atoms (highlighted in gold) that define the pore aperture of the largest member of the series, IRMOF-74-XI.

Visualizing the pores of MOFs by means of EM presents a considerable challenge because of their sensitivity to the electron beam. We examined members of this IRMOF-74 series with low-voltage high-resolution SEM (LV-HRSEM) (IRMOF-74-VII) and high-resolution transmission EM (HRTEM) (IRMOF-74-VII and IX). Preliminary results showed that we could clearly visualize the arrangement and the size of the pores in specimens of the crystals of those IRMOFs (Fig. 2, I to K). Ordered pores arranged in a hexagonal formation were resolved through both techniques, and the pore metrics are in agreement with those determined from x-ray crystallography. Through the HRTEM experiments, six-sided rings were observed when the incident electron beam was positioned along the *c* axis and thus parallel to the pore channels. Fast Fourier transform (FFT) analysis was performed on the centered square areas in the HRTEM images of IRMOF-74-VII and -IX (Fig. 2, J and K, insets). Six reflection spots corresponding to the 110 reflections were resolved from the FFT patterns, from which the *d*-spacing was measured (3.95 and 5.57 nm for IRMOF-74-VII and -IX, respectively). These values are in good agreement with the *d*-spacing values derived from the x-ray crystal structure analysis (4.59 and 5.69 nm for IRMOF-74-VII and -IX, respectively). The small deviations from x-ray crystal analysis can be attributed to the broad spot in the FFT analysis and the ultra-high vacuum condition used in the HRTEM experiment. Furthermore, through the HRTEM analysis images of the channel direction (*c* axis) were observed by placing the incident electron beam perpendicular to the channels [(*22*), section S5].

The unit cell, void volume, and pore aperture cover a wide range as the size of the organic link is increased (table S4). The void volume calculated by using the crystal structure data increased from 49 to 85% for the parent IRMOF-74-I to -XI. The pore aperture is defined as the length of the diagonal and the distance between the two opposite edges in the regular hexagonal cross section (Fig. 3A, atom-to-atom distance). This method is consistent with that previously used for referring to the pore aperture, and it was deployed here to facilitate comparison with reported values (*2*, *26*). The diagonal dimension of the pore aperture, based on the refined unit cell, increased from 19 Å in IRMOF-74-II to 98 Å in IRMOF-74-XI, with a discrete increment of nearly 6 Å as each phenylene unit was added. Furthermore, upon the addition of each phenylene unit there was an increase of 24 atoms in the ring size defining the pore aperture, leading to rings of 282 atoms in IRMOF-74-XI (Fig. 3B). This number of atoms far exceeds that defining the most open zeolites. In this series of IRMOFs, eight out of nine members (IRMOF-74-II to XI) have pore dimensions falling in the mesoporous region (>20 Å). Several other MOFs have been reported whose pore sizes are in this mesoporous region (*1*–*3*, *26*–*31*); however, their pore apertures are all exceeded by six members of this IRMOF series (IRMOF-74-IV to XI).

In order to assess the porosity of the IRMOFs and their architectural stability, Ar gas adsorption measurements at 87 K were performed. Initially, we carried out the activation procedures and characterization so as to ensure that the pores have been activated and free of guests. The solids of the IRMOFs were subjected to solvent exchange followed by evacuation, and in some cases treated with supercritical carbon dioxide, to obtain porous samples [(*22*), section S6]. These samples were studied by means of thermal gravimetric analysis, which showed no weight loss up to 300°C, confirming the high thermal stability of all the IRMOFs and indicating the absence of organic solvents from their pores. Successful removal of unreacted starting materials and organic solvent was further confirmed through ^{13}C cross-polarization/magic angle–spinning nuclear magnetic resonance [(*22*), section S6], elemental analysis, and Fourier transform infrared spectroscopy [(*22*), section S5]. Ar adsorption isotherms were measured on the activated samples of IRMOF-74-II to -XI (Fig. 4, A to D) [(*22*), section S7], each of which displays a Type IV isotherm that is typical of mesoporous materials (*8*). The magnitude of the relative pressure of the second step in the type IV isotherm is attributed to the increase in the effective energy of adsorption (pore-filling or condensation), in which higher pressures (P/P_0) are required for progressively larger pore sizes. Indeed, the starting point of the second step for IRMOF-74-II to -XI is observed at P/P_0 = 0.03, 0.12, 0.21, 0.30, 0.38, 0.46, 0.55, and 0.64, respectively. This gradual shift of the step position corresponds closely to the pore size expansion trend in the series. In addition, the pore sizes of these IRMOFs were examined by fitting nonlocal density functional theory models to the Ar adsorption isotherms. The estimated values are in line with the pore aperture metrics derived from the crystal structures [(*22*), section S7].

The pore volume in the frameworks is reflected in their Ar uptake capacity, which increases systematically from IRMOF-74-I to -XI as longer organic links are incorporated (440, 800, 990, 1310, 1520, 1320, 1680, 2000, and 2580 cm^3 g^{-1} at P/P_0 = 0.9, respectively; slightly lower uptake is observed in IRMOF-74-VI because of the use of Zn instead of Mg). The largest calculated pore volume in the series is for IRMOF-74-XI (3.3 cm^3 g^{-1}), which is near that of the recently reported ultrahighly porous MOF-210 (3.6 cm^3 g^{-1}) (*27*). In contrast, the highest Brunauer-Emmett-Teller (BET) surface area among the IRMOFs was observed in IRMOF-74-II, and the BET surface areas for IRMOFs with longer organic links showed even lower values because of the smaller geometric surface per volume (1350, 2510, 2440, 2480, 2230, 1600, 1800, 1920, and 1760 m^2 g^{-1} for IRMOF-74-I to -XI, respectively). Nevertheless, the surface areas are still much higher as compared with those found in mesoporous silica, porous carbon, and zeolites, thus providing more readily available surfaces for interaction with large guest molecules. The low density, which was also achieved in this IRMOF series, is not only attributable to the increase of open space but is a consequence of

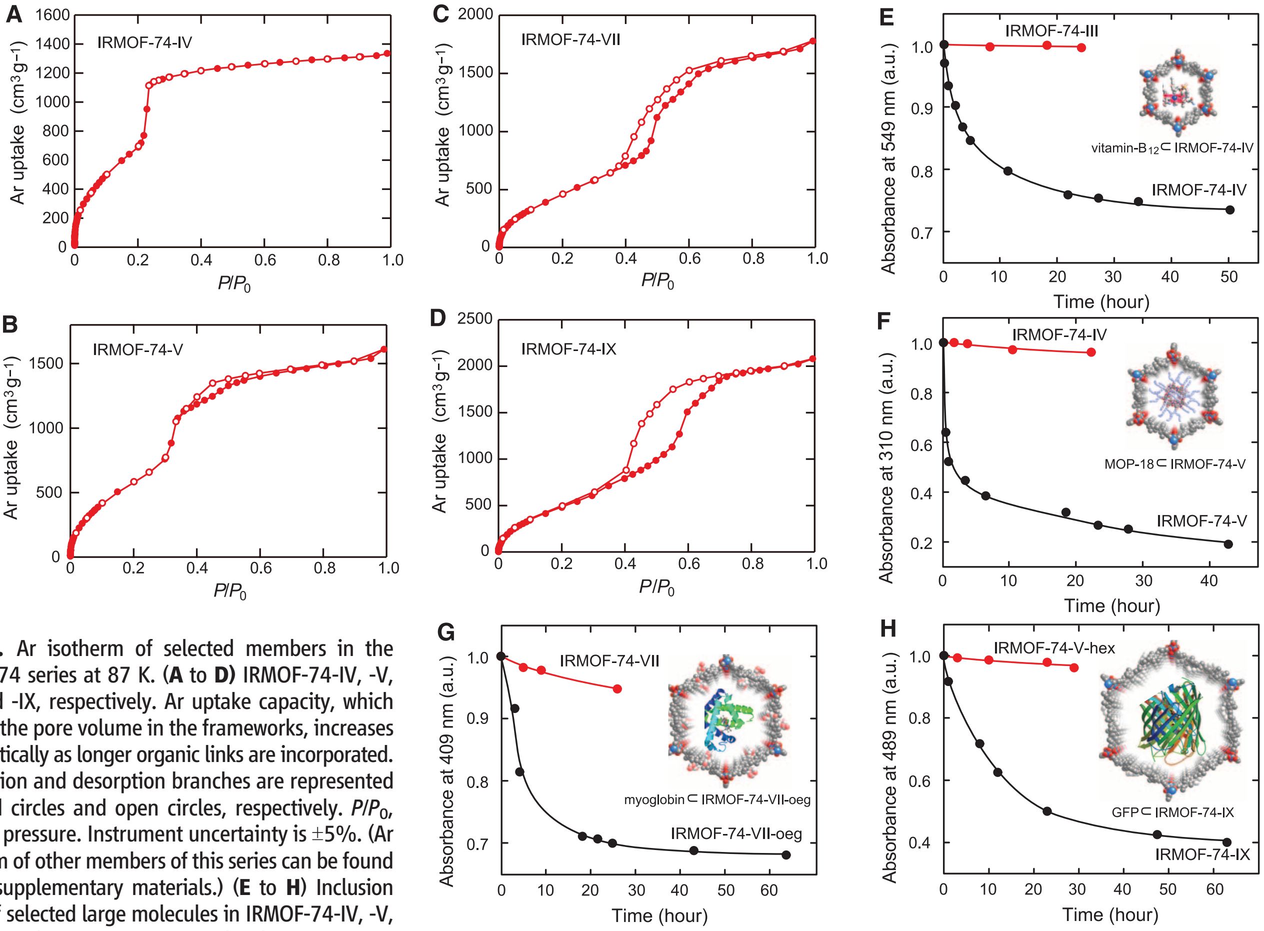

Fig. 4. Ar isotherm of selected members in the IRMOF-74 series at 87 K. (**A** to **D**) IRMOF-74-IV, -V, -VII and -IX, respectively. Ar uptake capacity, which reflects the pore volume in the frameworks, increases systematically as longer organic links are incorporated. Adsorption and desorption branches are represented by solid circles and open circles, respectively. P/P_0, relative pressure. Instrument uncertainty is ±5%. (Ar isotherm of other members of this series can be found in the supplementary materials.) (**E** to **H**) Inclusion study of selected large molecules in IRMOF-74-IV, -V, -VII-oeg and -IX series, respectively. This process was monitored through the decrease in absorbance at a selected wavelength as a function of contact time. For each measurement, the initial absorbance was normalized to 1.0. (Insets) Illustrations of the inclusion complex for each study.

the use of Mg, a metal with light weight, for the formation of the SBU. Seven of the eight new IRMOFs were constructed with Mg, including IRMOF-74-XI, which has the crystal density of $0.195\ g\ cm^{-3}$, the lowest known so far for a guest-free crystal at room temperature. There are several examples of crystalline materials reported with slightly lower framework density; however, they have not been proved to exist in their guest-free form (*32*, *33*).

Given the remarkable stability, ultrahigh porosity, and extremely large-pore-aperture characteristic of the IRMOF-74 series, we now have the ability to access a new size regime for the inclusion of large organic, inorganic, and biological molecules inside the pores of these IRMOF crystals. Preliminary measurements demonstrate the inclusion of large molecules into IRMOFs with appropriate pore apertures—specifically, vitamin B_{12} (largest size dimension of 27 Å) in IRMOF-74-IV, MOP-18 (inorganic spherical cluster with a diameter of 34 Å) (*34*) in IRMOF-74-V, myoglobin (globular protein with spherical dimensions of 21 by 35 by 44 Å) in IRMOF-74-VII-oeg, and GFP (barrel structure with diameter of 34 Å and length of 45 Å) in IRMOF-74-IX.

Typically, crystals of the desired IRMOF-74 were immersed in a solution containing the particular guest compound to be included. Activated crystals of IRMOF-74-IV were immersed in a 0.11 mM solution of vitamin B_{12}. The amount of vitamin B_{12} in the supernatant was measured with ultraviolet-visible (UV-Vis) spectrophotometry, and the characteristic absorbance at 480 nm was monitored over a period of 48 hours. The results are plotted in Fig. 4E, which clearly shows a continuous decrease of the amount of vitamin B_{12} in the supernatant. The same experiment was carried out, as a control, with IRMOF-74-III, whose pore aperture is smaller than IRMOF-74-IV and was not expected to show any uptake of vitamin B_{12}. This result was confirmed in that no decrease in absorbance was observed (Fig. 4E). Similar experiments were done for the inclusion of MOP-18 in IRMOF-74-V, myoglobin in IRMOF-74-VII-oeg, and GFP in IRMOF-74-IX (Fig. 4, F to H, respectively). For the solid resulting from the inclusion of MOP-18, an Ar adsorption isotherm at 87 K of a dried sample displayed a decrease in the step pressure as a result of inclusion into the pore [(*22*), section S8]. In the case of myoglobin, we functionalized the pores with a hydrophilic group (triethylene glycol mono-methyl ether, oeg) and observed substantial uptake by the corresponding IRMOF-74-VII-oeg because of myoglobin's hydrophilic surface. However, a negligible amount of myoglobin inclusion was observed in the control experiment, in which the pores were functionalized by hydrophobic hexyl chains, IRMOF-74-VII (Fig. 4F). For the control experiment in the GFP inclusion study, we used the hexyl chain functionalized IRMOF-74-V, termed IRMOF-74-V-hex, to provide a similarly hydrophobic pore environment to IRMOF-74-IX (Fig. 4G). Furthermore, GFP retained its folded structure when included in IRMOF-74-IX, as evidenced through confocal microscopy, which showed an unaltered characteristic fluorescence of GFP [(*22*), section S8]. It is remarkable that the crystallinity of the IRMOF materials is fully maintained throughout the inclusion process; the diffraction lines in the PXRD patterns of the included samples are coincident with those of the starting materials [(*22*), section S8].

References and Notes

1. Y. K. Park *et al.*, *Angew. Chem. Int. Ed.* **46**, 8230 (2007).
2. L. Ma *et al.*, *Nat. Chem.* **2**, 838 (2010).
3. M. Eddaoudi *et al.*, *Science* **295**, 469 (2002).
4. X. Lin *et al.*, *J. Am. Chem. Soc.* **131**, 2159 (2009).
5. N. L. Rosi *et al.*, *J. Am. Chem. Soc.* **127**, 1504 (2005).
6. P. D. C. Dietzel *et al.*, *Eur. J. Inorg. Chem.* **2008**, 3624 (2008).
7. S. A. Bagshaw *et al.*, *Science* **269**, 1242 (1995).
8. D. Zhao *et al.*, *Science* **279**, 548 (1998).
9. S. H. Joo *et al.*, *Nature* **412**, 169 (2001).
10. S. Inagaki *et al.*, *Nature* **416**, 304 (2002).
11. O. M. Yaghi *et al.*, *Nature* **423**, 705 (2003).
12. S. Kitagawa *et al.*, *Angew. Chem. Int. Ed.* **43**, 2334 (2004).
13. D. Bradshaw *et al.*, *Acc. Chem. Res.* **38**, 273 (2005).
14. J. S. Seo *et al.*, *Nature* **404**, 982 (2000).
15. Z. Wang, S. M. Cohen, *J. Am. Chem. Soc.* **129**, 12368 (2007).
16. B. D. Chandler *et al.*, *Nat. Mater.* **7**, 229 (2008).
17. O. Shekhah *et al.*, *Chem. Soc. Rev.* **40**, 1081 (2011).
18. M. Dincă *et al.*, *J. Am. Chem. Soc.* **128**, 16876 (2006).
19. V. Lykourinou *et al.*, *J. Am. Chem. Soc.* **133**, 10382 (2011).
20. N. L. Rosi *et al.*, *Angew. Chem. Int. Ed.* **114**, 294 (2002).
21. M. Lin *et al.*, *CrystEngComm* **13**, 776 (2011).
22. Materials and methods are available as supplementary materials on *Science* Online.
23. M. O'Keeffe, O. M. Yaghi, *Chem. Rev.* **112**, 675 (2012).
24. D. Hanss, O. S. Wenger, *Eur. J. Inorg. Chem.* **2009**, 3778 (2009).
25. S. T. Pasco, G. L. Baker, *Synth. Met.* **84**, 275 (1997).
26. X.-S. Wang *et al.*, *J. Am. Chem. Soc.* **128**, 16474 (2006).
27. H. Furukawa *et al.*, *Science* **329**, 424 (2010).
28. A. Sonnauer *et al.*, *Angew. Chem. Int. Ed.* **48**, 3791 (2009).
29. O. K. Farha *et al.*, *Nat. Chem.* **2**, 944 (2010).
30. X. Zhang *et al.*, *Angew. Chem. Int. Ed.* **50**, 5729 (2011).
31. B. Wang *et al.*, *Nature* **453**, 207 (2008).
32. H. M. El-Kaderi *et al.*, *Science* **316**, 268 (2007).
33. H. Furukawa *et al.*, *Inorg. Chem.* **50**, 9147 (2011).
34. H. Furukawa *et al.*, *J. Am. Chem. Soc.* **128**, 8398 (2006).

Acknowledgments: The research at UCLA was funded by BASF SE (Ludwigshafen, Germany) (synthesis of MOFs), the Center for Gas Separations Relevant to Clean Energy Technologies, an Energy Frontier Research Center (EFRC) funded by the DOE, Office of Science, Office of Basic Energy Sciences (U.S. DOE–BES) for adsorption (DE-SC0001015), and the U.S. Department of Defense, Defense Threat Reduction Agency for inclusion studies (HDTRA11-1-0018). The research conducted at Northwestern University was supported in part by the Non-equilibrium Energy Research Center, which is an EFRC funded by the U.S. DOE–BES (DE-SC0000989). We acknowledge the World Class University Program (R-31-2008-000-10055-0). We thank M. Zhao and D. Li from D. S. Eisenberg's group at UCLA for providing GFP and helpful discussions. Portions of this research were carried out at the Stanford Synchrotron Radiation Laboratory, a national user facility operated by Stanford University on behalf of the U.S. DOE–BES. Confocal laser scanning microscopy was performed at the California NanoSystems Institute Advanced Light Microscopy/Spectroscopy Shared Resource Facility at UCLA, supported with funding from NIH–National Center for Research Resources shared resources grant (CJX1-443835-WS-29646) and NSF Major Research Instrumentation grant (CHE-0722519). We acknowledge JEOL for providing their latest LV-HRSEM instrument. We thank M. Schibler, S. Wan, L. Wang, A. Sue, C. Stevens, C. Knobler, and J. Brown for their invaluable assistance. Z.L. acknowledges K. Suenaga at AIST, Tsukuba, Japan, for his encouragement. S.G. acknowledges the Swiss National Science Foundation for financial support. F.G. acknowledges funding by the Spanish Ministry of Education through the "Programa de Movilidad de Recursos Humanos del Plan Nacional de I-D+i 2008-2011." All data and images are available in the body of the paper or as supplementary materials. Crystallographic data for the reported crystal structures have been deposited at the Cambridge Crystallographic Data Centre via www.ccdc.cam.ac.uk with codes 841642 to 841651 (IRMOF-74-II to -XI, respectively).

Supplementary Materials
www.sciencemag.org/cgi/content/full/336/6084/1018/DC1
Materials and Methods
Figs. S1 to S51
Tables S1 to S6
References (*35*–*38*)

6 February 2012; accepted 6 April 2012
10.1126/science.1220131

Linking Petrology and Seismology at an Active Volcano

Kate Saunders,[1]* Jon Blundy,[1] Ralf Dohmen,[2] Kathy Cashman[1]

Many active volcanoes exhibit changes in seismicity, ground deformation, and gas emissions, which in some instances arise from magma movement in the crust before eruption. An enduring challenge in volcano monitoring is interpreting signs of unrest in terms of the causal subterranean magmatic processes. We examined over 300 zoned orthopyroxene crystals from the 1980–1986 eruption of Mount St. Helens that record pulsatory intrusions of new magma and volatiles into an existing larger reservoir before the eruption occurred. Diffusion chronometry applied to orthopyroxene crystal rims shows that episodes of magma intrusion correlate temporally with recorded seismicity, providing evidence that some seismic events are related to magma intrusion. These time scales are commensurate with monitoring signals at restless volcanoes, thus improving our ability to forecast volcanic eruptions by using petrology.

Zoned volcanic crystals preserve a record of magmatic processes over the lifetime of the crystal, from initial nucleation to final quenching upon eruption (*1*–*3*). Perturbations in magmatic variables (such as composition, volatile content, temperature, pressure, and oxidation state) can cause crystal zonation. The interplay of volatile loss through degassing and heating due to magma chamber recharge can result in complex textural patterns of crystal growth and dis-